Application of a finite difference computational model to the simulation of earthquake generated tsunamis

Article *in* Applied Numerical Mathematics · January 2013

CITATIONS
0

READS
464

5 authors, including:

Giorgos Alexandrakis
Foundation for Research and Technology - Hellas
66 PUBLICATIONS **760** CITATIONS
SEE PROFILE

Nikolaos A. Kampanis
Foundation for Research and Technology - Hellas
101 PUBLICATIONS **1,085** CITATIONS
SEE PROFILE

Costas E. Synolakis
University of Southern California
322 PUBLICATIONS **13,724** CITATIONS
SEE PROFILE

Applied Numerical Mathematics 67 (2013) 111–125

Contents lists available at ScienceDirect

Applied Numerical Mathematics

www.elsevier.com/locate/apnum

Application of a finite difference computational model to the simulation of earthquake generated tsunamis

Evangelia T. Flouri [a,b,*], Nikos Kalligeris [a,b], George Alexandrakis [a,c], Nikolaos A. Kampanis [a], Costas E. Synolakis [d,b,a]

[a] Institute of Applied and Computational Mathematics, FORTH, N. Plastira 100, Vassilika Vouton, GR-70013 Heraklion, Crete, Greece
[b] Department of Environmental Engineering, Technical University of Crete, GR-73100 Chania, Greece
[c] Department of Geography and Climatology, National and Kapodistrian University of Athens, Zographou, GR-15784 Athens, Greece
[d] Hellenic Center for Marine Research, Anavyssos, Attica, Greece

ARTICLE INFO

Article history:
Available online 17 June 2011

Keywords:
Tsunami
Long waves
Nonlinear shallow water equations
Splitting technique
Finite differences
Earthquake generated tsunami
Propagation
Runup
Inundation
Flow depth
Fault parameters estimation
Tsunami hazard

ABSTRACT

Tsunamis are long waves and commonly modeled with the shallow-water wave approximation of the equations of motion. The calculation of tsunami inundation remains after two decades of progress a vexing and temperamental computation exquisitely dependent on ad-hoc algorithms. We present computed results using, a splitting method in space to reduce this hyperbolic system in two successive hyperbolic systems, one for each primitive variable. Then, we use dispersive, Godunov type finite difference method and solve the equations in characteristic form. We use the methodology implemented in the code MOST to calculate inundation from four different earthquake scenarios for Heraklion, Greece. MOST has been repeatedly benchmarked. The scenarios are geophysical estimates of the source mechanisms of the 365 AD event, the largest known earthquake in the Eastern Mediterranean in the last two millenia. The earthquake scenarios used allow for defining the seafloor deformation resulting from the parent seismic motions and, after translating them to the water surface, they constitute the initial conditions for computations. We use high resolution bathymetric and topographic data to generate fine resolution grids used in the computations. Our practice allows for a precise identification of the onland inundation and the overland flow depths and currents during tsunami flooding in Heraklion. This is the first time such a quantitative study has been undertaken for Eastern Crete. We conclude that there is substantial hazard, and there is little difference among the four different seismic interpretations of the 365 AD earthquake.

1. Introduction

Tsunamis are rare events compared to other natural hazards. However, population growth along shorelines has increased the number and impact of tsunami disasters, as tsunamis can rapidly develop and grow in shallow coastal waters [3, 41]. They can be simulated effectively, therefore, as long waves whose propagation and inundation is modeled by the nonlinear shallow water equations. Tsunamis are usually generated by an earthquake induced dislocation of the seabed which displaces a large mass of water. Submarine and aerial landslides and volcanoes also generate tsunamis.

* Corresponding author at: Institute of Applied and Computational Mathematics, FORTH, N. Plastira 100, Vassilika Vouton, GR-70013 Heraklion, Crete, Greece.
E-mail address: flouri@iacm.forth.gr (E.T. Flouri).

0168-9274/$30.00 © 2011 Published by Elsevier B.V. on behalf of IMACS.
doi:10.1016/j.apnum.2011.06.003

Tsunamis have very different kinematic characteristics from wind waves. Wind waves usually have period of 5–20 seconds and a wavelength of about 100 to 200 meters, [20], while tsunami waves can have periods and wavelengths exceeding 10 minutes and 100 km (in the open sea) respectively. Their long wavelength is the basis for studying tsunamis as shallow-water waves, i.e., the ratio between the water depth and the wavelength is small. In coastal areas, smaller water depths diminish the wave velocity, and increase the wave height. This is known as shoaling; a tsunami with heights of the order of a few centimeters in the open seas, can develop a height of several meters near shore. The tsunami evolution nearshore is affected by local bathymetric features, while its inundation is quite dependent on onshore topography.

A considerable effort has been made in developing tsunami simulation models and support tsunami hazard assessment for coastal areas worldwide, cf. e.g. [3,28,29,41]. Risk assessment and coastal planning depend on a set of tsunami damage metrics such as the (i) time of the tsunami wave arrival in the site of interest, (ii) extreme water levels (maximum wave height) in the flooded area, (iii) the inundation area, (iv) water depths and velocities in the inundated zones, among others.

The flow field established by a tsunami wave is an incompressible flow with a free surface, theoretically described by the Navier–Stokes equations. However, a fully 3D configuration has a high computational cost, since then the size of the spatial domain in realistic cases can be very large and flow patterns of different length scales exist in the flow. Quantitative approximations of the flow field are invariably based on approximations of the equations of motion.

Near shore propagation of long wave assumes hydrostatic pressure variation and then only the two horizontal momentum equations remain to be solved. A further simplification is performed by averaging velocities over the depth. The depth-averaged formulation results in the nonlinear shallow water (NSW) equations [22]. They provide accurate results at a relatively low computational cost compared with fully 3D approaches, and they have been extensively used to model propagation and runup of shallow water long waves, flooding and drying problems and flow in coastal regions.

Finite difference methods have been extensively used for numerical solutions of the NSW equations. They apply in a straightforward manner to structured Cartesian grids; the use of a curvilinear transformation of coordinates allows handling of more complex geometries. This results in partial differential equations with additional derivatives as well as complicated boundary conditions in the transformed domain. Finite difference schemes have been used in one- and two-dimensional models for long waves runup, usually based on the nonconservative (primitive) form of the NSW equations. While numerical solutions of the NSW had been proposed for a least a decade earlier [46], were the first to have solved the 1+1 problem with inundation computations and validated it with the set of benchmark problems that are now standard [42]. In [46] the characteristic form of the NSW equations is solved using finite difference methods; in [47] the one-dimensional model of [46] is extended to two dimensions and solved by a splitting scheme. A different FD scheme is presented in [21], also including flooding and drying of the initially dry bed, and also benchmarked with the circular island data of [4]. Reviews of finite difference methods used to simulate long waves are found in [19] and [24].

The finite element method relies upon a variational formulation (cf. [34]) of the equations of fluid motion and has been applied to river and dam beak flood propagation, river inflows and tidal flows, wave propagation and advancing fronts. Recent work [33,48] included discretization of the finite elements of the NSW equations based on the discontinuous Galerkin formulation. The use of a discontinuous Galerkin formulation has many advantages, such as higher-order accuracy and more sharp evaluation of shocks. In [16] and [50] long wave runup models have been developed based on Eulerian and Lagrangian formulations of the underlying equations, respectively. Further reference to the method is found in [18,24,49], and the references therein.

Finite volume approaches [1,12], have been also used for the discretization of the 2D NSW equations. The method applies to both structured and unstructured grids. The hyperbolicity of the NSW equations allows for the application of numerical methods used in computational fluid mechanics for compressible flows. Godunov-type finite volume approaches use the conservative form of the equations to relate integral averages of the conserved variables and inter-cell fluxes, and the wave propagation information (upwind) to compute inter-cell fluxes. Triangular, unstructured grid formulations of Godunov-type NSW models have been adopted further for grid refinement in irregular domains [9].

In the present work, the hazard from an earthquake generated tsunami, that following the AD 365 earthquake in particular, has been simulated using the numerical model MOST, now in use by the National Oceanic and Atmospheric Administration (NOAA) of the US for real time forecasts [3]. In Section 2 the model problem is shown and the numerical scheme is introduced as applied. In Section 3 the MOST model, is described. In Section 4 the case study on the simulation of the tsunami generated by the AD 365 earthquake, off the western Cretan coast, is considered. The reconstruction of the seismic event is used to provide initial conditions. Different sets of parameters and associated values, that depict the uncertainty of the fault parameters determination, are used to set four different scenarios to derive the initial condition based on the induced seafloor displacement by the scenario earthquakes. These scenarios are representative of the AD 365 historical event, cf. [23,30,35,37], respectively; they are expected to model effectively the epistemic uncertainty of the fault parameters for this specific event. The computational domain is described by high resolution bathymetric data around the island of Crete and topographic data selected by aerial imaging. A hierarchy of nested telescoping grids is constructed. This enables the reconstruction of the behavior of the wave with improved resolution near shore and over the initially dry coastline. The results are shown in the form of inundation maps and plots of various tsunami damage metrics. Since the northern coast of Crete is densely populated (a population which grows significantly during summer months), a tsunami hazard assessment is of value for emergency evacuation planning. Therefore, different descriptions of the seismic source (through the use of different source parameters values) have been used to model the epistemic uncertainty of the source and its influence on

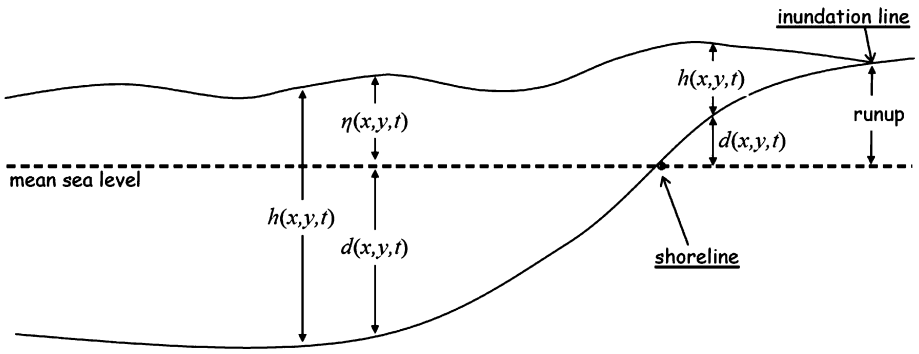

Fig. 1. Basic notations.

the tsunami impact. Lower and upper bounds of the inundation are provided to bound the tsunami hazard from a possible repeat of this event.

The closing Section 6 includes a discussion of the results and conclusions regarding the quality of the simulations produced and the estimated tsunami hazard.

2. Mathematical model and discretization technique

The two-dimensional (2D) nonlinear shallow water equations (NSW) used to model long wave propagation are

$$\left.\begin{aligned} &h_t + (uh)_x + (vh)_y = 0 \\ &u_t + uu_x + vu_y + gh_x = gd_x \\ &v_t + uv_x + vv_y + gh_y = gd_y \end{aligned}\right\} \tag{1}$$

where $h = \eta(x, y, t) + d(x, y, t)$ is the fluid depth, $\eta(x, y, t)$ is the amplitude of the wave, $d(x, y, t)$ is the bed topography function (undisturbed water depth),[1] $u(x, y, t)$ and $v(x, y, t)$ are the velocities in longitude (x) and latitude (y), respectively, and g is the gravitational constant, cf. Fig. 1.

The water is considered as an incompressible fluid, the pressure as hydrostatic, vertical accelerations negligible and waves as nondispersive. In many practical applications these are reasonable assumptions under the shallow water hypothesis [41].

Initial conditions for (1) will be provided through source terms in the right-hand side of the system. The generation of a tsunami, due to bottom displacement, as in the case of an earthquake generated tsunami, is expressed by a fast change in the seafloor and/or onshore topography. Therefore let

$$\begin{aligned} &d(x, y, t) = d_0(x, y, t), \quad 0 \leqslant t \leqslant t_0, \\ &d(x, y, t) = d(x, y), \qquad t \leqslant t_0 \end{aligned}$$

with t_0 small enough, and d_0 a rapidly varying function of t. This rapid variation of the source term establishes a distribution for $h(x, y, t_0)$, $u(x, y, t_0)$ and $v(x, y, t_0)$. This distribution can be considered as the initial conditions for (1).

An application of the fractional step method [1,5,7], reduces the problem (under the assumption of mild coupling mechanisms between the two space variables) to solving two consecutive one-dimensional problems. Therefore, the following quasi-linear hyperbolic systems need to be solved

$$\left.\begin{aligned} &h_t + (uh)_x = 0 \\ &u_t + uu_x + gh_x = gd_x \\ &v_t + uv_x = 0 \end{aligned}\right\}, \qquad \left.\begin{aligned} &h_t + (vh)_y = 0 \\ &v_t + vv_y + gh_y = gd_y \\ &v_t + vv_y = 0 \end{aligned}\right\}. \tag{2}$$

Both systems in (2) have three real and distinct eigenvalues, therefore they may be written in characteristics form. For example, the system on the left of (2) reduces to

$$\begin{aligned} &(p_1)_t + \lambda_1 (p_1)_x = gd_x, \\ &(p_2)_t + \lambda_2 (p_2)_x = gd_x, \\ &(p_3)_t + \lambda_3 (p_3)_x = 0 \end{aligned} \tag{3}$$

with

[1] The dependence on t of the bed topography d will be used to provide an initial condition for the wave.

$$p_1 = u + 2\sqrt{gh}, \qquad p_2 = q - 2\sqrt{gh}, \qquad p_3 = v, \tag{4}$$

the Riemann invariants of the system, and

$$\lambda_1 = u + \sqrt{gh}, \qquad \lambda_2 = u - \sqrt{gh}, \qquad \lambda_3 = u, \tag{5}$$

the associated eigenvalues. In terms of calculating tsunami inundation, these equations in this form were first presented by [47].

Eq. (3) is discretized by a Godunov type scheme using a second-order accurate explicit finite difference scheme in space and a first-order accurate in time. The overall scheme reads as follows:

$$\frac{\Delta_t p_i^n}{\Delta t} + \frac{1}{2\Delta x}\left[\lambda_i^n(\Delta_{-x} + \Delta_x)p_i^n - \frac{\Delta t}{\Delta x}\lambda_i^n \Delta_x\left(\lambda_i^n \Delta_{-x} p_i^n\right)\right] = \frac{g}{2\Delta x}\left[(\Delta_{-x} + \Delta_x)d_i^n - \frac{\Delta t}{\Delta x}\lambda_i^n \Delta_x \Delta_{-x} d_i^n\right] \tag{6}$$

where $f_i^n = f(x_i, t_n)$, Δx is space step, Δt is time increment, and

$$\begin{aligned} \Delta_t f_i^n &= f(x_i, t_n + \Delta t) - f(x_i, t_n), \\ \Delta_x f_i^n &= f(x_i + \Delta x, t_n) - f(x_i, t_n), \\ \Delta_{-x} f_i^n &= f(x_i, t_n) - f(x_i - \Delta x, t_n), \end{aligned} \tag{7}$$

in the interior of the computational domain.

The boundary conditions that render Eq. (3) well-posed in a bounded domain are deduced according to the value of the Froude number $\mathbf{Fr} = u/\sqrt{gh}$. The number of boundary conditions for the Riemann invariants p_i, $i = 1, 2, 3$, should be equal to the outgoing characteristics (those corresponding to the λ_i's with the same sign). Since here (under the shallow water approximation) $\mathbf{Fr} < 1$, $\lambda_1 > 0$ and $\lambda_2 < 0$, in the computational domain, while λ_3 changes sign arbitrarily. Therefore, one or two boundary conditions (depending on the sign of λ_3 on this boundary) are needed on each boundary, for the incoming characteristics and the associated Riemann invariants. Boundaries are characterized as reflective or transmissive, and proper formulations of the necessary boundary conditions are used, respectively, as in [45].

As an example, the characteristic defined by λ_2 is incoming on the right boundary, therefore p_2 is set by the boundary condition. However, p_1 should be computed from (3) using an appropriate discretization on the boundary. This is accomplished by applying the upwind scheme

$$(p_1)_b^{n+1} = (p_1)_b^n - \frac{\Delta t}{\Delta x}\left[\lambda_1^n\left(\Delta_{-x}(p_1)_b^n\right) - g\left(\Delta_{-x} d_b^n\right)\right], \tag{8}$$

where the subscript b indicates values on this boundary.

Near the shoreline, the evolution of the wave on the dry bed needs the use of a moving boundary for its calculation. Proper handling of the wet–dry front in a finite difference context, discussed in [45–47]. The use of variable (time dependent) meshlength during overland flow, guarantees that the front is placed where the horizontal extension of the last wet point, meets the bed topography. Inundation computation with MOST, therefore, uses this moving boundary conditions to calculate the evolution of the wave on the initially dry bed.

Other approaches to handle the wet–dry front evolution, also suitable for finite volume or finite element formulations, are shown e.g. in [5–8]. In, e.g., [10], the technique of [5] and [6] has been successfully extended to cooperate with a high-order, cell-centered finite volume scheme.

3. The MOST numerical model

Here, the MOST (Method of Splitting Tsunamis) numerical model [46,47] is used. The model allows for a direct simulation of the tsunami, i.e. models all three phases of its evolution: the generation, the propagation in the open sea, and the inland penetration (inundation). It has been extensively effectively validated through comparisons with benchmark test cases and field data; and tsunami hazards have been reproduced in reliable form [42,49].

The simulation by MOST model of an earthquake-generated tsunami in a realistic environment requires detailed description of the seismic source mechanism for the generation phase, and high resolution bathymetric and topographic data to produce the grid for the evolution and inundation phases.

Simulation of onshore inundation requires appropriate finer nested grids. Digital Elevation Models (DEM) of different resolution that specify bathymetry and topography within an established (x, y) coordinate system are thus mapped to a finite difference grid used as input to MOST calculations. The inner resolution data set, referred to as Grid C, has the smallest horizontal coverage and defines the target or area of principal interest for the inundation study. The outer, coarsest data set, Grid A, covers the largest area and is used in the propagation phase calculation and defines outflow boundary. The intermediate data set, Grid B, provides a transition region to improve the accuracy of MOST inundation calculations. Because runup/rundown calculations are performed for Grid C, detailed dry land topographical data is required.

During shoaling wavelengths become shorter. Therefore, calculations on a uniform grid throughout the whole computational domain suffer either loss of accuracy in the near shore field, or numerical instabilities if very fine grids are used. Either

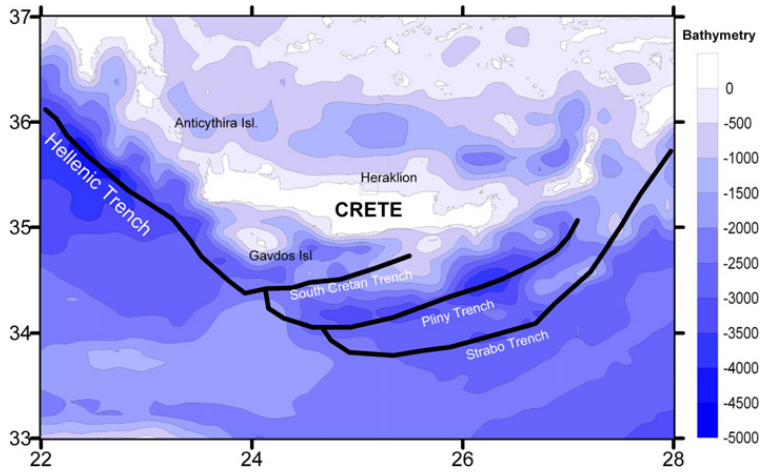

Fig. 2. Schematic presentation of the major faults in the West and South of Crete.

approach does not produce consistent resolution, as argued in [46]. A variable grid in each direction is used. Variable grid can create consistent resolution for one-dimensional domains, or for a cylindrical two-dimensional domain, when the depth is changing predominantly along one direction [47]. To model tsunami propagation in areas with complex bathymetries containing complicated shoreline patterns and islands, an additional nested grid is used for the nearshore computations. The nested grid has finer grid-spacing for an efficient computation of the shorter waves in the near shore area. In MOST, an algorithm to automatically create extra grid points for the areas where depth is less than a certain value, is used. Computed values are interpolated on the boundaries between the grids every time step to provide a continuous flow of information between the areas. This approach allows for a computation in large complicated areas with a minimum loss of accuracy due to inconsistent resolution of the finite-difference grid.

The generation phase in MOST model uses the vertical surface displacement caused by the seismic event [17,26], to provide the initial condition of the NSW equations for the propagation phase.

4. Case study

In the present study, the impact of an earthquake generated tsunami is evaluated, using seismic fault parameters attributed to the AD 365 event as discussed earlier. The individual areas selected for performing detailed runup simulation are the coastline of Heraklion district, in the north of Crete (Fig. 2). Crete is in the southern Aegean Sea, an area of high seismicity on the edge of the Hellenic Arc subduction zone. Seismicity in this region is related to both the north–south convergence between Africa and Europe, and the extension within the Aegean Sea province [44]. The 21 July 365 AD earthquake occurred SW of Crete [35,37,38], with estimated magnitudes $M \approx 8.5$. It produced significant uplift in western Crete, inferred to have reached up to 9 m in some locales [31,32,35].

4.1. Grid generation

The main data sources used for the bathymetry–topography reconstruction of the area are: (a) bathymetric and topographic data of 1 min resolution from GEBCO (General Bathymetric Chart of the Oceans) of the British Oceanographic Data Centre, (b) bathymetric data courtesy of the Hellenic Navy Hydrographic Service, and (c) Digital Terrain Models (DTMs) for the selected site produced by photogrammetric analysis of stereo aerial images of high resolution (DEM format corrected by a pair of digital stereographic aerial photos in a 2 m grid with horizontal accuracy of 0.2 m, and elevation accuracy of 0.4 m). All data were checked and merged according to a common and consistent georeference using a Geographic Information System (ArcGIS v.9 platform of ESRI). Overlapping features, caused by the merging of data from different sources that was derived by different methodologies and of different dates, were corrected based on the resolution of the source and the most recent time. In this procedure standard tools (such as the Spatial Analyst and 3D Analyst extensions) of ArcGIS were used to produce a new file containing all the corrected data, topographic and bathymetric. By interpolating the file, the grids that were necessary for the MOST model inputs was created following the convention that $d(x, y) > 0$ in the sea, while $d(x, y) < 0$ on land. The extracted nested grids for the city of Heraklion are shown in Fig. 3. The spatial resolution of the grids is shown in Table 1.

4.2. Tsunami source parameters

For the AD 365 historical event, the epistemic uncertainty of the fault parameters is high. Thus, four different scenarios of fault parameters sets were used to bound the tsunami hazard.

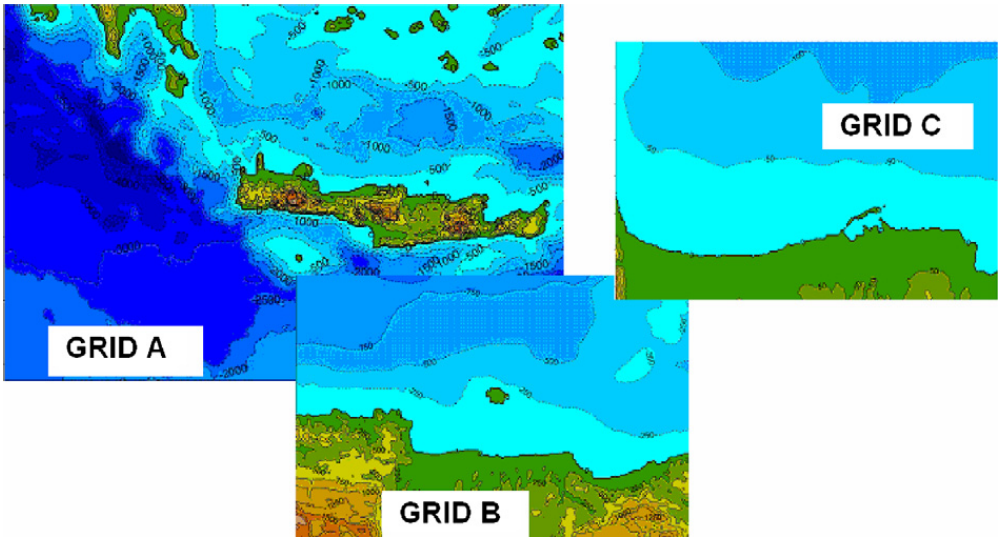

Fig. 3. Grids A, B and C used for the tsunami simulations in the present study, focusing in the area of Heraklion.

Table 1
Discretization parameters used for the numerical model (MOST).

Grid A	coarse	$\Delta x = \Delta y = 0.01^\circ = 1113.2$ m
Grid B	intermediate	$\Delta x = \Delta y = 0.00166^\circ = 184.7912$ m
Grid C	fine	$\Delta x = \Delta y = 0.00027^\circ = 30.0564$ m

Scenario S1 is extracted from [23]. The characteristics of the source were selected so as to fit a set of data on raised shorelines that have been attributed to coseismic vertical displacement [13,31,32,39]. Radiocarbon dating bracketed the date of this seismic event and led to the conclusion that the palaeoshorelines were raised from a single seismic event, the earthquake of AD 365. Fault dislocation modeling [26], allowed testing of different source characteristics and selection of the solution that best fits the field data. Strike and dip[2] were taken parallel to the orientation of the subduction plane and were kept constant through the iterative process. Rake was taken parallel to the plate motion and the seismogenic layer capable of producing earthquakes of the size of AD 365 was taken to be between 5 and 60 km. By keeping the aforementioned source parameters constant and having to solve for fault rupture area, slip magnitude and source location, a source mechanism was selected, with an estimated earthquake magnitude of $M_w = 8.4$, which produces a vertical surface displacement field that best-fits the recorded coastal uplift data.

Scenario S2 is that proposed in [30] and it is a fault model associated with the shallow dipping subduction of the eastern Mediterranean oceanic lithosphere beneath south Aegean microplate. It is based on correlation between calculated surface displacement and observed surface deformation on the landward portion of the Hellenic subduction zone. The fault area is divided in a number of subfaults segments and a simple elastic model defines the coseismic dislocation. The displacement pattern is complicated due to a non-uniform slip on the fault considered, in order to simulate rapid decrease of surface deformation in neighboring islands. In this model, the largest slip values are assigned onto the subfaults whose geographical position is near to the maximum reported surface displacements. The slip magnitude is different for each the subfault varying from 0 to 25 m, with an average value of 8.9 m. This scenario is in agreement with the observation that earthquakes in great subduction zones usually initiate towards the down-dip edge of the fault, and they expand substantially along strike and up dip but far less in the down-dip direction, with the principal epicenter occurring near the edges of the focal region. This has been the case with the 11 March 2011 Tohoku, Japan tsunami.

Scenario S3 is that of [35]. Following similar methodology as in the studies above, this source is based on field measurements of the uplift of palaeoshorelines and information from the distribution of earthquakes in the region to further constrain the location of the fault that caused the AD 365 earthquake. In [35] the authors modeled slip for candidate faults, with fixed strike (315) and depth (< 45 km), cropping out between the Mediterranean Ridge and the coast of Crete to find that the best fit to the uplift data is obtained for a fault that crops out near the Hellenic Trench. The best-fitting fault has a length of 100 km, slip is 20 ± 5 m to a depth of 45 km, and dip of $30 \pm 5^\circ$; these parameters produce uplift that matches field observations and measurements on Antikythira and produce no vertical displacement on the island of Gavdos, matching observations of no uplift/subsidence observation on the island.

Scenario S4 was proposed in [37]. Again, following similar methodology, the author focused his search for the best-fitting model on a steep thrust south of Crete, being the only fault candidate to produce no uplift in Gavdos and Kythira. The main difference with the former solutions is that the author did not select any seismological parameters a priori, nor

[2] For a concise definition of the fault parameters see [27].

Table 2
The four seismic scenarios.

Scenarios	Bibliographic reference	Depth (km)	Length (km)	Width (km)	Dip (deg)	Strike (deg)	Rake (deg)	Slip (m)
S1	[23] (Lorito et al., $M_w \approx 8.4$)	5	130	86	35	314	90	17.5
S2	[30] (Papadimitriou and Karakostas)	50	160	80	35	315	90	8.9[c]
S3	[35] (Shaw et al., $M_w \approx 8.5$)	45	100	80[a]	30	315	90[b]	20
S4	[37] (Stiros, $M_w \approx 8.5$)	70	105	100	40	292.5	90[b]	16

[a] Value derived from scaling formulas.
[b] Values producing maximum vertical displacement, not directly mentioned in the associated references cited in the first column.
[c] Average value.

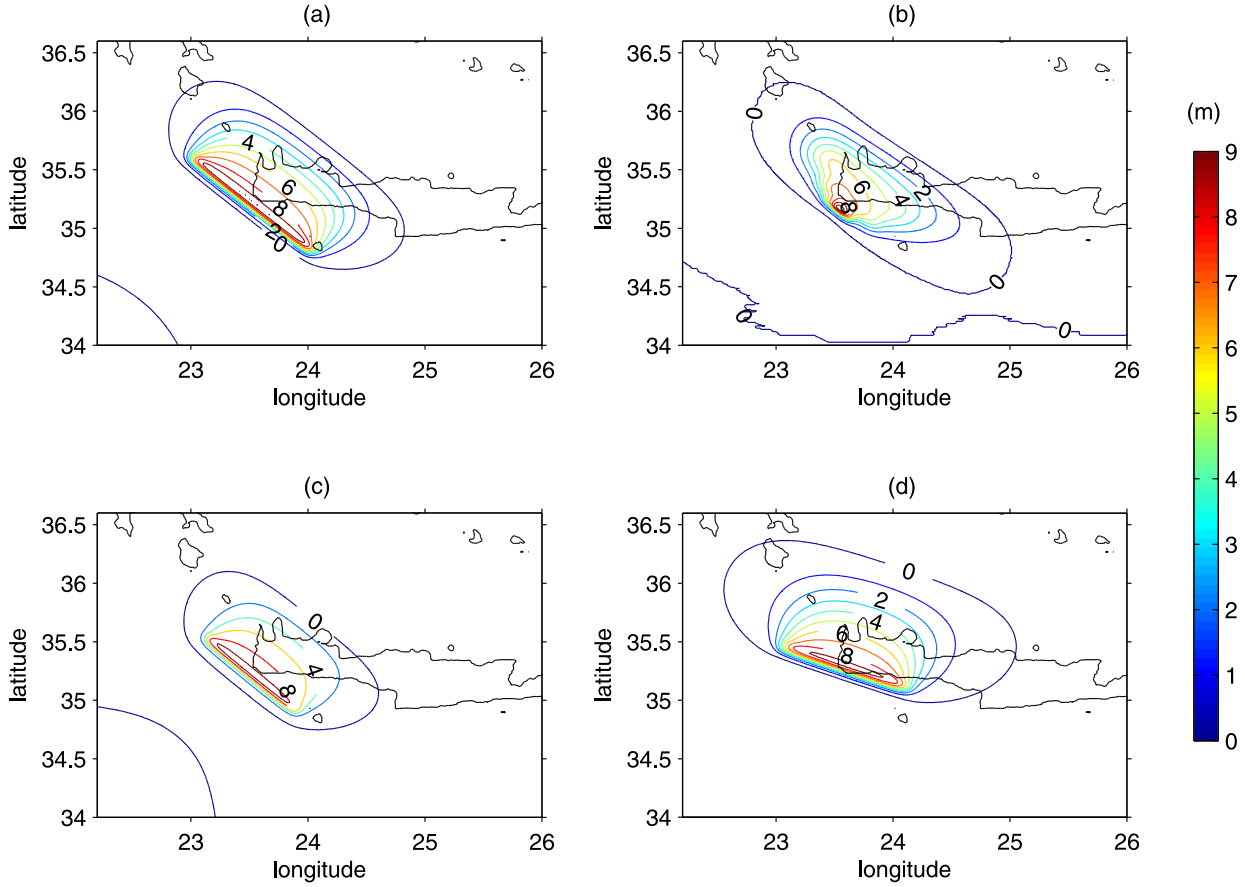

Fig. 4. Contours of uplift predicted for the fault using elastic dislocation analysis for the four scenarios S1–S4 in subplots (a)–(d) respectively.

did he constrain the solution by the strike of the Aegean Arc and the depth of the seismogenic layer. The author cites recent studies that show evidence which indicate micro-earthquake in depths greater than 90 km along the Hellenic Arc and argues that his solutions yield better fitting to the field data, while the characteristics of the source are realistic.

All four scenarios describe the observed coastal uplift, through different combinations of fault parameters varying in the rupture area length and width, location, which are in agreement with qualitative archaeological findings. Given that it is impossible to quantitatively locate the event, the initial location was chosen based on the best fit of the uplift contours as estimated in the four scenarios, listed in Table 2.

The initial conditions are constructed from the vertical surface displacement, calculated by the linear elastic dislocation theory applied to a rectangular uniform fault plane [25]. The rupture is assumed to occur almost instantaneously, and since the water is incompressible, the water–surface deformation mimics the seafloor deformation. The elastic model is used to provide the vertical deformation of the earth surface caused by the fault movement. Since the duration of the movement is very short compared to the period of the long water waves, the ground motion during an earthquake does not affect the evolution of the tsunami much. The whole process amounts in the computation of (a) the static vertical displacement by simulating an elastic halfspace (not including the sea column) with an inner seismic source [17,25], and (b) the propagation of the tsunami wave over the incompressible inviscid ocean, by a hydrodynamic model.

Surface dislocation due to a rupture along a fault is expressed in terms of a rectangular area – a region of ocean bottom bisected by the fault trace, with an orientation determined by the strike angle; a dip; a rake angle of the fault plane; and the ocean floor slip magnitude (dislocation) along the fault plane trace. The values of all these parameters follow the

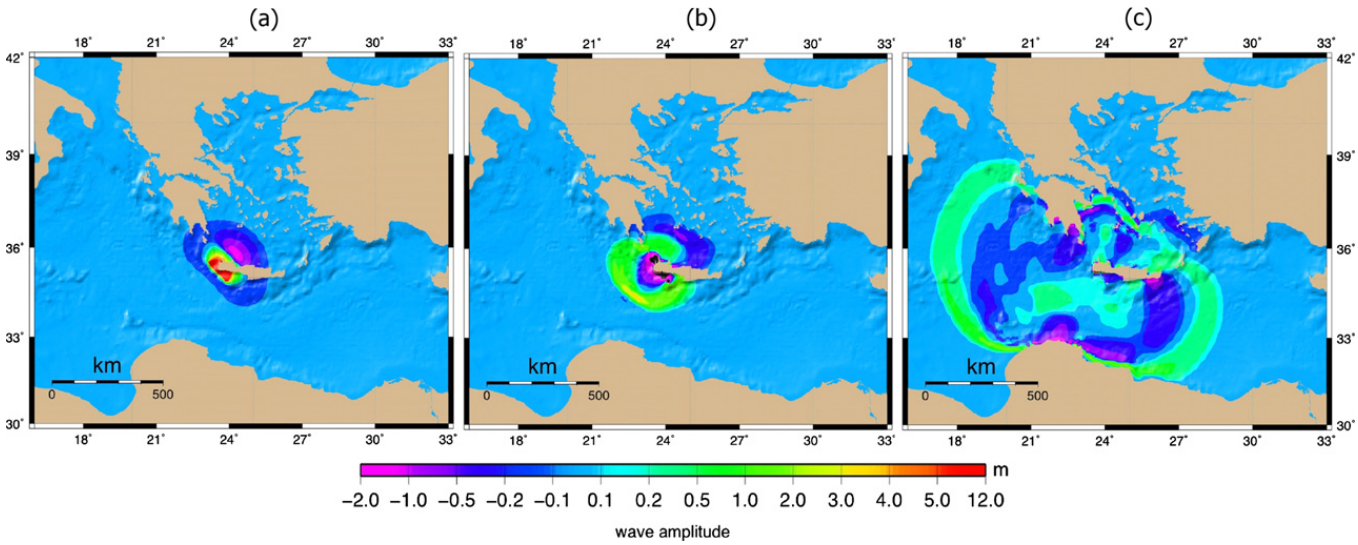

Fig. 5. Tsunami wave amplitude for scenario S3 at (a) $T_0 + 10$ min, (b) $T_0 + 12$ min, and (c) $T_0 + 50$ min.

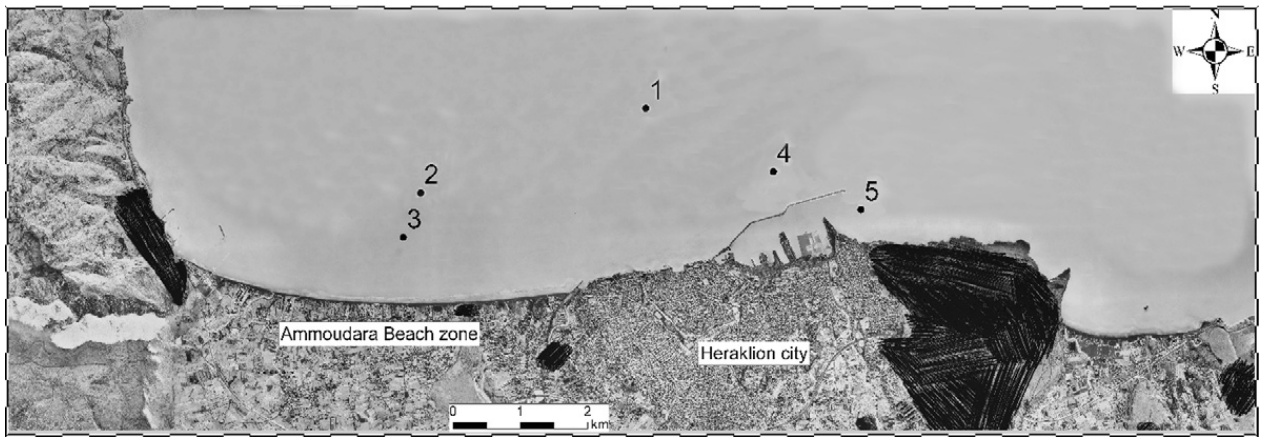

Fig. 6. A map of the Heraklion area with numerical wave gauges shown.

estimations of scenarios S1–S4. In order to model the spatial distribution of the variable slip for the case of scenario S2, the rectangular area is divided in 128 equal segments (subfaults), and in each segment a different value of slip amount is assigned following [30] (see Fig. 3, p. 303 of [30]). In Fig. 4, the contours of uplift calculated using the approach of [26] for displacements and the rupture characteristics of the four scenarios are plotted.

The four scenarios will be used to exploit the variability of the tsunami hazard that has been inferred for the AD 365-like event. This might be considered as a preliminary approach to a probabilistic tsunami hazard assessment [15]. However, even this simplified approach may provide a rough estimation of the induced hazard in relation to the epistemic uncertainty of the source parameters. This is of practical interest. We observed that variability in local runup can occur even for scenarios with the same seismic moment and slightly different source parameters, even for a location like Heraklion, about 150 km from the seismic source on the other side of the island [14].

5. Estimation of propagation and runup

A numerical simulation was at first performed for a wider area of Eastern Mediterranean using coarse bathymetric and topographic data; this is a test to the initial source parameters and also provides an estimation of the geographical extend of the area influenced by the propagation. In Fig. 5 snapshots of the wave amplitude in time $T_0 + 10$ s (a), $T_0 + 12$ min (b) and $T_0 + 50$ min (c), are shown for a representative scenario (S3). T_0 denotes the time when the seismic rupture develops (and establishes therefore the initial condition of values for the dependent variables). The results show strong impact in areas like North Africa and Peloponnesus, consistent with historical records [11,36].

In the sequel, the full tsunami simulation (including inundation) was performed, for all four scenarios selected, using the set of nested grids (see Fig. 3) that focuses to the individual area of interest. A $\Delta t = 0.64$ s was used for the stability of the computation.

In Fig. 7 the tsunami wave height in time is shown, for 5 gauges placed offshore the city of Heraklion at the locations depicted in Fig. 6. Arrival times of the tsunami waves (since tsunami is not a single wave but rather a series of waves), as

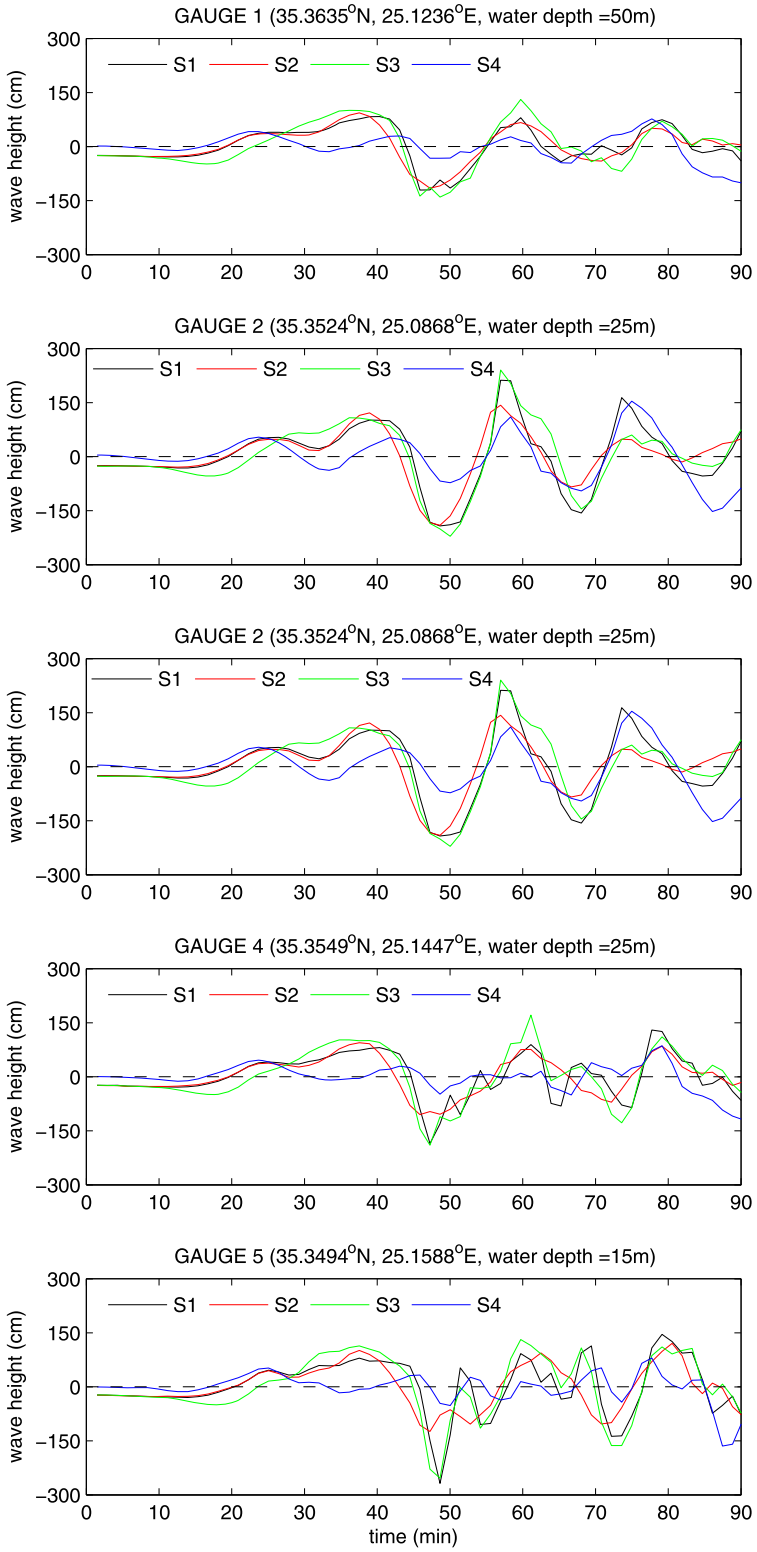

Fig. 7. Tsunami wave amplitude versus time for the five gauges shown in Fig. 6.

well as the initial formation of the tsunami approaching the coast can be deduced from Fig. 7. At first, a leading depression wave [43], that causes the shoreline to withdraw appears, while the first positive wave reaches the coast in less than 20 min. As can be seen clearly, that in almost all cases the first positive wave is not the highest. In the sequel, the results were projected in a digital map in order to show the inland penetration of the tsunami waves (inundation map).

The production of inundation maps plays an important role to the mitigation of tsunami hazards. Such maps are useful in assessing the population, structures and facilities exposed at risk and are helpful in planning evacuations [2].

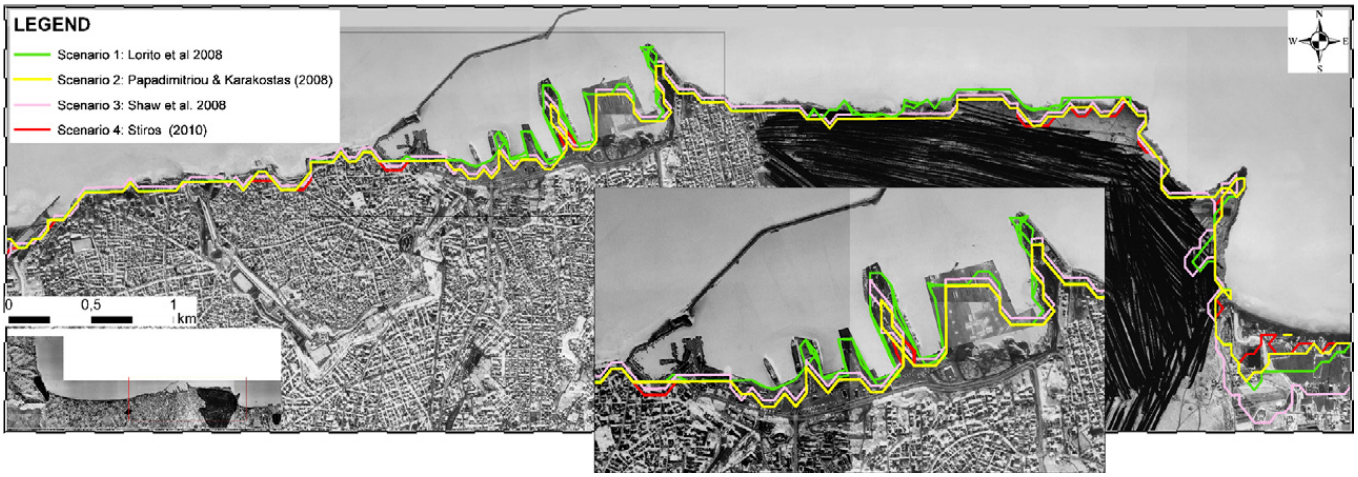

Fig. 8. Tsunami inundation lines for the four scenarios for Heraklion, shown on an aerial photo.

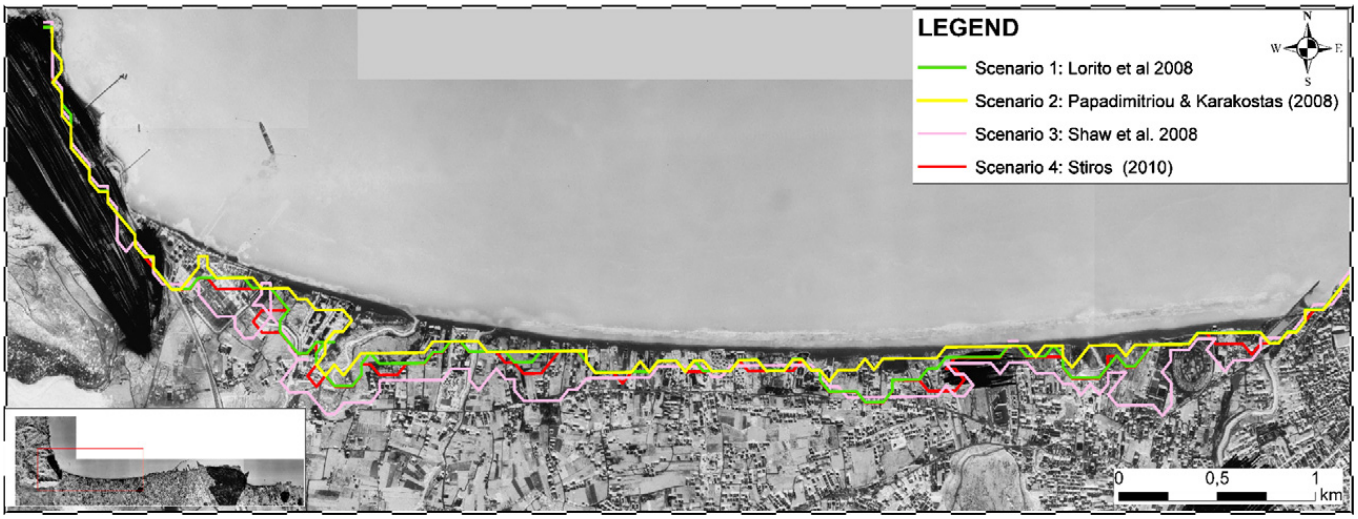

Fig. 9. Tsunami inundation lines for the four scenarios at the coastline of Ammoudara, West of Heraklion.

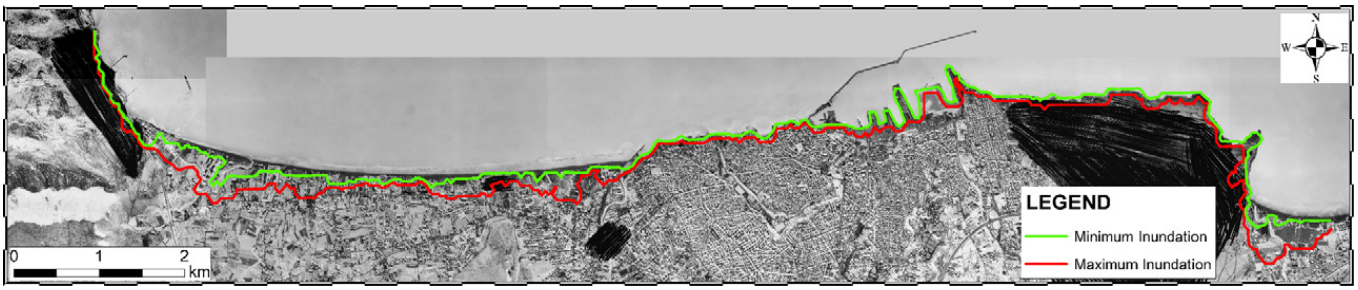

Fig. 10. The maximum and minimum inundation for coastline of Heraklion and Ammoudara, superposed on an aerial photo.

In Figs. 8 and 9 all four inundation lines (one for each scenario) are superimposed on a satellite image for the main part of the sea front and port of Heraklion, and of Ammoudara area in the city's western coastal suburbs, respectively. It is evident from Fig. 8 that most of the coastal areas are flooded, while the commercial harbor and beaches located at the western side suffer the largest inundation and damage. Scenarios S3 and S4 show an overall deeper inland penetration and appear to give the more catastrophic version of the event. Scenario S4 seems to have the worst impact in the largest part of the coastal area of Heraklion. A significantly deeper penetration in Karteros bay (east of Heraklion) is shown by scenario S3, cf. Fig. 8. Scenario S3 also shows the deepest inland penetration in Ammoudara district (west of Heraklion), cf. Fig. 9. The maximum and the minimum inland penetration derived from all four scenarios is shown in Fig. 10.

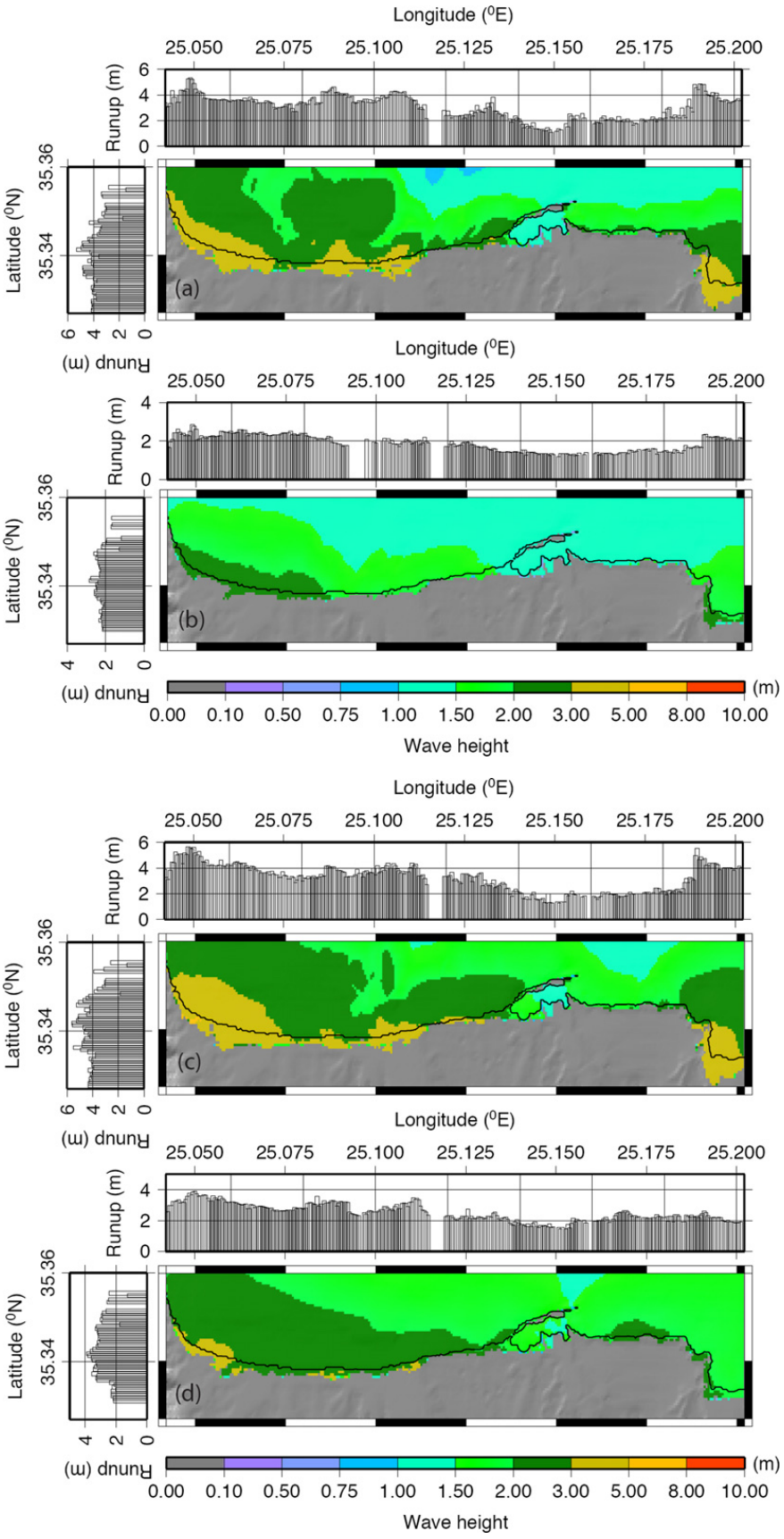

Fig. 11. Maximum wave elevation and runup calculated for scenarios S1–S4 in subplots (a)–(d), respectively.

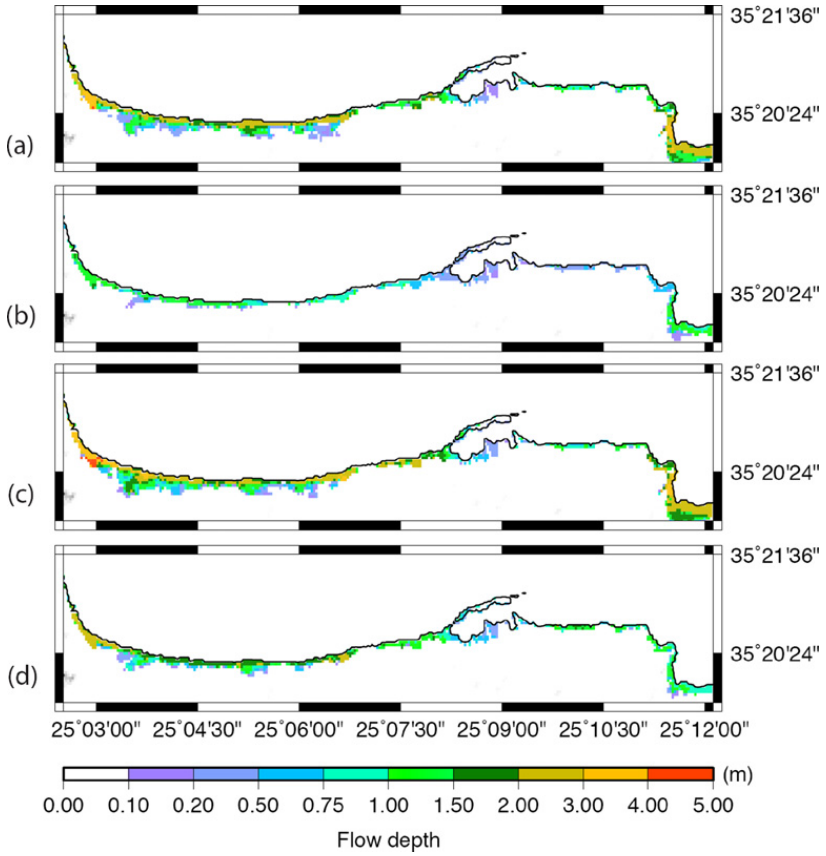

Fig. 12. Maximum flow depth calculated for scenarios S1–S4 in subplots (a)–(d), respectively.

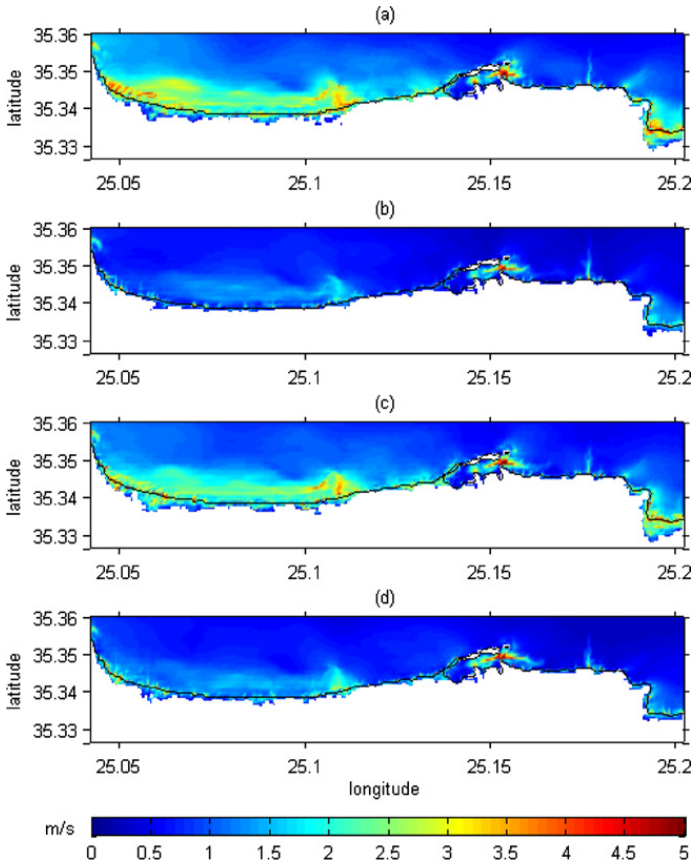

Fig. 13. Maximum current speed calculated for scenarios S1–S4 in subplots (a)–(d) respectively.

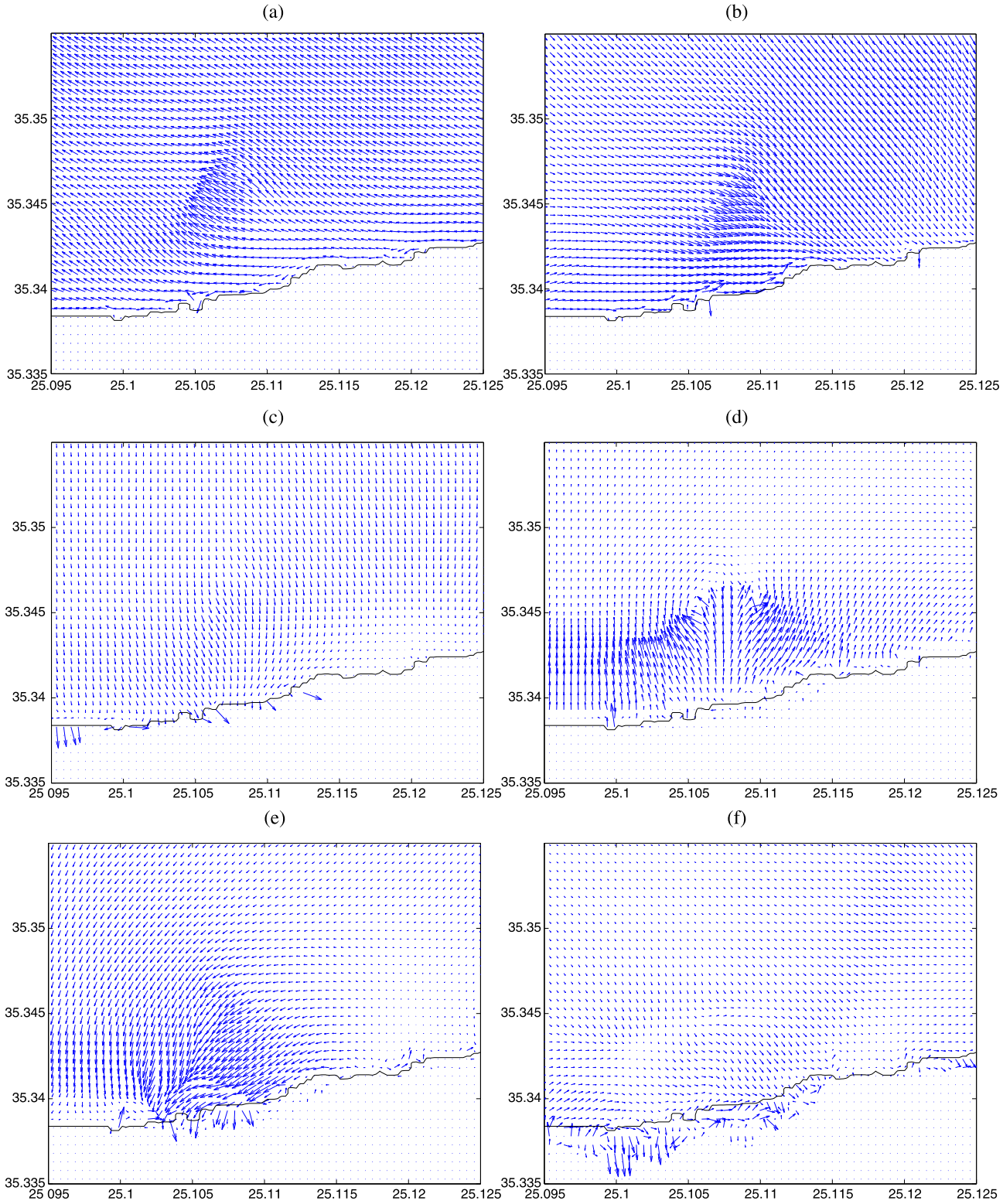

Fig. 14. Velocity vectors from scenario S3 for time (a) $T = 0$ h, (b) $T = 0.5$ h, (c) $T = 0.6$ h, (d) $T = 0.8$ h, (e) $T = 0.9$ h, (f) $T = 1.0$ h at the Giofyros river estuary.

Tsunami damage metrics [40], are presented next, as follows:

(a) The *maximum wave elevation* defined as $\max_t \eta(x, y, t)$ and is plotted in Fig. 11, for the wider area of Heraklion (Grid C). In the side plots the *runup* value is plotted, which represent the elevation of the inundation line.
(b) The *maximum flow depth*, defined as $\max_t h(x, y, t)$, plotted in Fig. 12 for all inland grid points of Grid C. The areas that seem to be most vulnerable, in the sense that the maximum flow depth exceeds 2 m, are the western coastal areas, while the maximum calculated flow depth value exceeds 4 m.

(c) The *maximum current speed*, defined as $\max_t \sqrt{u^2(x, y, t) + v^2(x, y, t)}$. In Fig. 13 the maximum current speed is plotted for the area of Grid C. Here, we note that the velocities vectors may have very strong variations, as it can be seen in Fig. 14, where the velocity vectors from the representative scenario S3 are shown for time $T = 0$ h, 0.5 h, 0.6 h, 0.8 h, 0.9 h, 1.0 h at the coast in the proximity of Giofyros river estuary, west of Heraklion.

Tsunamis can generate large onshore currents and cause dramatic damage to structures and move large objects far inland, as most recently witnessed during the 11 March 2011 Japan tsunami. In order to identify zones of potentially high tsunami hazard risk, it is important to introduce metrics that characterize the tsunami impact and reflect the distribution of forces over the entire impacted area. It is worth emphasizing that planning based solely on inundation maps of maximum wave height could be dangerously misleading since regions of high currents do not always correspond to regions of high wave height. For example, as the tsunami evolves over dry land, the flow depth decreases up to the point of maximum runup, and the velocity of the shoreline tip becomes zero. During rundown the flow depth remains small, but the velocity can be substantial.

6. Conclusions

The NSW equations were used to simulate the generation, evolution and inundation by tectonic tsunamis in the Southern Aegean Sea. A split-step finite difference based discretization was used for numerical integration. The case study considered is that of the tsunami generated by the AD 365 earthquake, NW of Crete, the largest known seismic event in the Eastern Mediterranean. The propagation and inundation as calculated are compatible with historic accounts of the tsunami impact, underscoring the robustness of our methodology and MOST. The epistemic uncertainty in the estimation of the seismic parameters was addressed by using four different scenarios, estimated 1600 post facto. Results are compared for all cases, and we provide upper and lower bounds of the estimated inundation, for selected areas of interest. The potential regional tsunami hazard appears substantial for coastal areas in Heraklion. Finally, we report that this scenario and the maps presented here were the basis of a large European Union civil defense exercise that took place in Crete in October 2011.

Acknowledgements

This study was supported by the EU (DG ENV.A3) project POSEIDON: *Earthquake followed by Tsunami in the Mediterranean Sea*, under contract No. 070401/2009/534369/SUB/A3 to the Institute of Applied and Computational Mathematics of the Foundation for Research and Technology-Hellas, and to grant CMS 0928905 by the National Science Foundation of the US to Professor Costas Synolakis.

References

[1] R. Abgrall, Computational methods for compressible flow problems, in: V.V. Shaidurov, O. Pironneau (Eds.), Computational Methods and Algorithms, in: Encyclopedia of Life Support Systems (EOLSS), Developed under the Auspices of the UNESCO, Eolss Publishers, Oxford, UK, 2003.
[2] A. Barberopoulou, J.C. Borrero, B. Uslu, M.R. Legg, C.E. Synolakis, A second generation of tsunami inundation maps for the State of California, Pure Appl. Geophys. 168 (2011) 1–14, doi:10.1007/s00024-011-0293-3.
[3] E.N. Bernard, H.O. Mofjeld, V.V. Titov, C.E. Synolakis, F.I. González, Tsunami: scientific frontiers, mitigation, forecasting and policy implications, Philos. Trans. R. Soc. A 364 (2006) 1989–2007.
[4] M.J. Briggs, C.E. Synolakis, G.S. Harkins, Tsunami runup on a conical island, in: Proc., Waves-Physical and Numerical Modelling, International Association for Hydraulic Research, Delft, The Netherlands, 1994, pp. 446–455.
[5] P. Brufau, P. García-Navarro, M.E. Vázquez-Cendón, Zero mass error using unsteady wetting–drying conditions in shallow flows over dry irregular topography, Internat. J. Numer. Methods Fluids 45 (2004) 1047–1082.
[6] P. Brufau, M.E. Vázquez-Cendón, P. García-Navarro, A numerical model for the flooding and drying of irregular domain, Internat. J. Numer. Methods Fluids 39 (2002) 247–275.
[7] M.J. Castro, A.M. Ferreiro, J.A. García-Rodriguez, J.M. González-Vida, J. Macías, C. Parés, M.E. Vázquez-Cendón, The numerical treatment of wet/dry fronts in shallow flows: application to one-layer and two-layer systems, Math. Comput. Modelling 42 (2005) 419–439.
[8] M.J. Castro, J. González–Vida, C. Parés, Numerical treatment of wet/dry fronts in shallow flows with a modified Roe scheme, Math. Models Methods Appl. Sci. 16 (2006) 897–931.
[9] A.I. Delis, N.A. Kampanis, Numerical flood simulation by depth averaged free surface flow models, in: Achim Sydow (Ed.), Environmental Systems, in: Encyclopedia of Life Support Systems (EOLSS), Developed under the Auspices of the UNESCO, Eolss Publishers, Oxford, UK, 2009, http://www.eolss.net [retrieved August 17, 2009].
[10] A.I. Delis, M. Kazolea, N.A. Kampanis, A robust high resolution finite volume scheme for the simulation of long waves over complex domains, Internat. J. Numer. Methods Fluids 56 (2008) 419–452.
[11] A. Di Vita, Archaeologists and earthquakes: the case of 365 AD, Ann. Geofis. 38 (1995) 971–976.
[12] F. Dubois, An introduction to finite volume methods, in: V.V. Shaidurov, O. Pironneau (Eds.), Computational Methods and Algorithms, in: Encyclopedia of Life Support Systems (EOLSS), Developed under the Auspices of the UNESCO, Eolss Publishers, Oxford, UK, 2003.
[13] N. Flemming, Holocene eustatic changes and coastal tectonics in the Northeast Mediterranean: implications for models of crustal consumption, Trans. Roy. Soc. Lond. 289 (1978) 405–458.
[14] E.L. Geist, Complex earthquake rupture and local tsunamis, J. Geophys. Res. 107 (B5) (2002) 2086, doi:10.1029/2000JB000139.
[15] F.I. González, E.L. Geist, B. Jaffe, U. Kânoglu, H. Mofjeld, C.E. Synolakis, V.V. Titov, D. Arcas, D. Bellomo, D. Carlton, T. Horning, J. Johnson, J. Newman, T. Parsons, R. Peters, C. Peterson, G. Priest, A. Venturato, J. Weber, F. Wong, A. Yalciner, Probabilistic tsunami hazard assessment at Seaside, Oregon, for near- and far-field seismic sources, J. Geophys. Res. 114 (2009) C11023, doi:10.1029/2008JC005132.
[16] T.C. Gopalakrishnan, C.C. Tung, Run-up of non-breaking waves: a finite-element approach, Coast. Engrg. 4 (1980) 3–32.

[17] V.K. Gusiakov, Static displacement on the surface of an elastic space, in: Ill-Posed Problems of Mathematical Physics and Interpretation of Geophysical Data, VC SOAN SSSR, Novosibirsk, 1978, pp. 23–51 (in Russian).
[18] P. Helluy, F. Golay, J.-P. Caltagirone, P. Lubin, S. Vincent, D. Drevard, R. Marcer, P. Fraunie, N. Seguin, S. Grilli, A.-C. Lesage, A. Dervieux, O. Allain, Numerical simulations of wave breaking, ESAIM: Math. Model. Numer. Anal. 39 (2005) 591–607.
[19] F. Imamura, Review of tsunami simulation with finite difference method, in: H. Yeh, P. Liu, C. Synolakis (Eds.), Long-Wave Runup Models, World Scientific Publishing Co., Singapore, 1996, pp. 25–42.
[20] B. Kinsman, Wind Waves – Their Generation and Propagation on the Ocean Surface, Dover Publications, Inc., 1965.
[21] P.L.-F. Liu, Y.-S. Cho, M.J. Griggs, U. Kânoğlu, C.E. Synolakis, Runup of solitary wave on a circular island, J. Fluid Mech. 302 (1995) 259–285.
[22] P.L.-F. Liu, C.E. Synolakis, H. Yeh, Impressions from the first international workshop on long wave runup, J. Fluid Mech. 229 (1991) 675–688.
[23] S. Lorito, M.M. Tiberti, R. Basili, A. Piatanesi, G. Valensise, Earthquake-generated tsunamis in the Mediterranean Sea: Scenarios of potential threats to Southern Italy, J. Geophys. Res. 113 (2008) B01301, doi:10.1029/2007JB004943.
[24] C.L. Mader, Numerical Modeling of Water Waves, CRC Press, Boca Raton, 2004.
[25] L. Mansinha, D.E. Smylie, The displacement fields of inclined faults, Bull. Seismol. Soc. Amer. 61 (1971) 1433–1440.
[26] Y. Okada, Surface deformation due to shear and tensile faults in a half space, Bull. Seismol. Soc. Amer. 75 (1985) 1135–1154.
[27] E.A. Okal, A student's guide to teleseismic body-wave amplitudes, Seismol. Res. Lett. 63 (1992) 169–180.
[28] E.A. Okal, C.E. Synolakis, N. Kalligeris, Tsunami simulations for regional sources in the South China and adjoining seas, Pure Appl. Geophys. 168 (2011) 1153–1173.
[29] E.A. Okal, C.E. Synolakis, B. Uslu, N. Kalligeris, E. Voukouvalas, The 1956 earthquake and tsunami in Amorgos, Greece, Geophys. J. Int. 178 (2009) 1533–1554.
[30] E.E. Papadimitriou, V.G. Karakostas, Rupture model of the great AD 365 Crete earthquake in the southwestern part of the Hellenic Arc, Acta Geophys. 56 (2008) 293–312, doi:10.2478/s11600-008-0001-6.
[31] P. Pirazzoli, J. Laborel, S. Stiros, Earthquake clustering in the Eastern Mediterranean during historical times, J. Geophys. Res. 101 (B3) (1996) 6083–6097.
[32] P. Pirazzoli, J. Thommeret, Y. Thommeret, J. Laborel, L. Montagionni, Crustal block movements from Holocene shorelines: Crete and Antikythira (Greece), Tectonophysics 68 (1982) 27–43.
[33] J.-F. Remacle, S. Soares Frazao, X. Li, M.S. Shephard, An adaptive discretization of shallow-water equations based on discontinuous Galerkin methods, Internat. J. Numer. Methods Fluids 52 (2006) 903–923.
[34] J.-H. Saiac, Finite element method, in: V.V. Vladimir, V. Shaidurov, O. Pironneau (Eds.), Computational Models and Algorithms, in: Encyclopedia of Life Support Systems (EOLSS), Developed under the Auspices of the UNESCO, Eolss Publishers, Oxford, UK, 2004.
[35] B. Shaw, N.N. Ambraseys, P.C. England, M.A. Floyd, G.J. Gorman, T.F.G. Higham, J.A. Jackson, J.-M. Nocquet, C.C. Pain, M.D. Piggott, Eastern Mediterranean tectonics and tsunami hazard inferred from the AD 365 earthquake, Nature Geosci. 1 (2008) 268–276.
[36] S.C. Stiros, The AD 365 Crete earthquake and possible seismic clustering during the 4–6th centuries AD in the Eastern Mediterranean: a review of historical and archaeological data, J. Struct. Geol. 23 (2001) 545–562.
[37] S.C. Stiros, The 8.5^{+} magnitude, AD365 earthquake in Crete: Coastal uplift, topography changes, archaeological and historical signature, Quat. Internat. 216 (2010) 54–63.
[38] S. Stiros, S. Papageorgiou, Seismicity of western Crete and the destruction of the town of Kisamos at AD365: archaeological evidence, J. Seismol. 5 (2001) 381–397.
[39] S. Stiros, A. Drakos, A fault-model for the tsunami-associated, magnitude $\leqslant$ 8.5 Eastern Mediterranean, AD365 earthquake, Z. Geomorphol. 146 (2006) 125–137.
[40] C.E. Synolakis, Tsunami and seiche, in: W.F Chen, C. Scawthorn (Eds.), Earthquake Engineering Handbook, CRC Press, 2004, pp. 9-1–9-90.
[41] C.E. Synolakis, E.N. Bernard, Tsunami science before and beyond Boxing Day 2004, Philos. Trans. R. Soc. A 364 (2006) 2231–2265.
[42] C.E. Synolakis, E.N. Bernard, V.V. Titov, U. Kânoğlu, F.I. González, Validation and verification of tsunami numerical models, Pure Appl. Geophys. 165 (2008) 2197–2228.
[43] S. Tadepalli, C.E. Synolakis, The run-up of N waves on sloping beaches, Proc. R. Soc. Lond. A 445 (1994) 99–112.
[44] T. Taymaz, J. Jackson, R. Westaway, Earthquake mechanisms in the Hellenic Trench near Crete, Geophys. J. Int. 102 (1990) 695–731.
[45] V.V. Titov, Numerical modeling of long wave runup, PhD dissertation, University of Southern California, 1997.
[46] V.V. Titov, C.E. Synolakis, Modeling of breaking and nonbreaking long wave evolution and runup using VTCS-2, J. Waterway, Port, Coastal, Ocean Eng. 121 (1995) 308–316.
[47] V.V. Titov, C.E. Synolakis, Numerical modeling of tidal wave runup, J. Waterway, Port, Coastal, Ocean Eng. 124 (1998) 157–171.
[48] J.-W. Wang, R.-X. Liu, Combined finite volume-finite element method for shallow water equations, Comput. & Fluids 34 (2005) 1199–1222.
[49] H. Yeh, P.L.-F. Liu, C.E. Synolakis (Eds.), Long-Wave Run-Up Models, World Scientific Publishing, Singapore, 1996.
[50] J.A. Zelt, The run-up of nonbreaking and breaking solitary waves, Coast. Engrg. 15 (1991) 205–246.